**PAPER**

Check for updates

# Tunable lattice dynamics and dielectric functions of two-dimensional Bi$_2$O$_2$Se: striking layer and temperature dependent effects†

Yafang Li,[a] Kai Dai,[a] Lichen Gao,[a] Jinzhong Zhang, [iD] *[a] Anyang Cui, [iD] [a] Kai Jiang,[a] Yawei Li, [iD] [a] Liyan Shang,[a] Liangqing Zhu[a] and Zhigao Hu [iD] *[a,b]

Two-dimensional (2D) Bi$_2$O$_2$Se semiconductors with a narrow band gap and ultrahigh mobility have been regarded as an emerging candidate for optoelectronic devices, whereas the ambiguous phonon characteristics and optical properties still limit their future applications. Herein, high-quality centimeter-scale 2D Bi$_2$O$_2$Se films are successfully synthesized to disclose the lattice dynamics and dielectric functions under the control of thickness and temperature. It has been demonstrated that the stronger electrostatic Bi–Se interactions result in a stiffened phonon vibration of thicker Bi$_2$O$_2$Se layers. Three excitons ($E_a$, $E_b$, and $E_c$) exhibit significant red shifts with layer stacking. Interestingly, the dielectric properties in the visible-near infrared region ($E_a$ and $E_b$) are dominated by the combined effect of the joint density of states and mass density, whereas the dielectric properties in the ultraviolet region ($E_c$) are dominated by the exciton effect. Furthermore, the temperature-sensitivity of the phonon frequency and exciton transition energies is revealed to be layer-dependent. In particular, the optical response of $E_b$ excitons exhibits a prominent dependence on temperature, which indicates a promising optical modulation by temperature in the visible spectrum. This study enriches the knowledge about phonon dynamics and dielectric properties for 2D Bi$_2$O$_2$Se, which provides an essential reference for high-performance related optoelectronic devices.

## Introduction

Due to the remarkable properties derived from the distinctive lattice symmetry and modulated electronic structure, two-dimensional (2D) materials, such as 2D perovskites,[1] black phosphorus,[2] and transition metal dichalcogenides,[3] have attracted considerable attention in recent years. However, the excellent properties including a suitable band gap, ultrahigh light responsivity, fast response speed and environmental stability are difficult to achieve simultaneously in one material system, which is one of the main challenges for the practical applications of 2D materials. As a typical bismuth-based oxychalcogenide material, layered Bi$_2$O$_2$Se shows an adjustable band gap, which decreases from ~2.09 eV for the monolayer to

~0.8 eV for the bulk, an ultrahigh Hall mobility value as high as ~2.9 × 10$^4$ cm$^2$ V$^{-1}$ s$^{-1}$ at 1.9 K, large current on/off ratios (>10$^6$), and brilliant stability in air.[4] The narrow electronic band gap combined with the high mobility underlies the high sensitivity and ultrafast photoresponse of 2D Bi$_2$O$_2$Se-related applications.[5–9] In addition, due to its wide-ranging solar absorption, Bi$_2$O$_2$Se is also regarded as a suitable photocatalyst which is verified by the photocatalytic degradation of methylene blue dye in visible light.[10] The unique electronic structure and abundant physical characteristics have made Bi$_2$O$_2$Se a superior candidate for numerous practical applications, like photodetection, photovoltaic devices, biomedicine, *etc*.

The interlayer interaction in multilayer 2D materials dramatically affects the electronic structures, chemical bonding, and lattice vibrations, which initiates the development of effective methods to modulate electronic, optical, mechanical, and vibrational properties under the control of layer thickness. Different from van der Waals-based 2D materials, the interlayer interaction in Bi$_2$O$_2$Se is contributed by the weak electrostatic interaction of Bi–Se bonds. Hence, the changes in the Bi–Se bond properties will influence lattice parameters and the corresponding electronic structure. Even though great strategies and mechanisms have been studied to modulate the physical properties of Bi$_2$O$_2$Se, the ambiguous phonon charac-

*[a]Technical Center for Multifunctional Magneto-Optical Spectroscopy (Shanghai), Engineering Research Center of Nanophotonics & Advanced Instrument (Ministry of Education), Department of Physics, School of Physics and Electronic Science, East China Normal University, Shanghai 200241, China. E-mail: jzzhang@ee.ecnu.edu.cn , zghu@ee.ecnu.edu.cn; Fax: +86-21-54342933; Tel: +86-21-54345150*
*[b]Collaborative Innovation Center of Extreme Optics, Shanxi University, Taiyuan, Shanxi 030006, China*

teristics and dielectric functions still limit its future applications.[11–14] On one hand, the evolution of phonon dynamics with 2D $Bi_2O_2Se$ thickness is ambiguous. Based on group-theory analysis and first-principles calculations, Cheng *et al.* have predicted that the Raman active modes in $Bi_2O_2Se$ will stiffen as the interlayer interaction increases from the monolayer to bulk,[15] whereas the evolution has not been clarified in the experiment. Therefore, further investigation is crucial for clarifying the correlations between the structure and physical properties. On the other hand, the optical properties of 2D $Bi_2O_2Se$, including absorbance and the third-harmonic generation effect, have been reported, which indeed provide some physical information.[16,17] Nevertheless, the fundamental optical constants, which play essential roles in the quantitative design of $Bi_2O_2Se$-based photoelectric devices, are yet to be reported. In addition, the self-heating effect derived from the relaxation process in practical devices and the necessity of various applications at extreme temperatures should be considered. Therefore, the investigation under external perturbation is essential for disclosing the thermal stability and is conducive to the future development of $Bi_2O_2Se$-based devices. Finally, to meet the high standards of advanced electronics and optoelectronics, the material is required to have a suitable size, thickness, and other characteristics. However, it is still a huge challenge to extend the lateral size of $Bi_2O_2Se$ films at the atomic level with a low-cost synthesis.[18–20]

In this work, high-quality centimeter-scale layer-controlled ultrathin $Bi_2O_2Se$ films were successfully prepared. The lattice symmetry, optical properties, and electronic structure were systematically investigated under the control of layer number and temperature. The stiffening of the Raman-active phonon behavior was revealed, which can be attributed to the stronger interlayer interactions. Three excitons ($E_a$, $E_b$, and $E_c$) exhibit a significant redshift trend with increasing thickness due to the band gap narrowing. As the layer number increases, the imaginary part of the dielectric functions in $E_a$ and $E_b$ exhibit a layer-dependent increment, while showing an inverse tendency from the transition $E_c$. It can be explained by the combined effect of the joint density of states and mass density in the low-energy region, and the domination of the exciton effect in the high-energy region. Moreover, the significant temperature dependence of the $E_b$ exciton in $Bi_2O_2Se$ indicates an excellent optical modulation by temperature in the visible spectral region. This work can strengthen the fundamental understanding of the lattice variation and dielectric functions of $Bi_2O_2Se$ and further provide important guidance for designing and modulating $Bi_2O_2Se$-based optoelectronic devices.

## Experimental

### Growth of 2D $Bi_2O_2Se$ films

The centimetre-scale 2D $Bi_2O_2Se$ films with variable layers were deposited on *c*-plane sapphire substrates using a two-zone chemical vapor deposition (CVD) system; the schematic is displayed in Fig. 1a. 0.5 g of high-purity Se metal (99.999%)
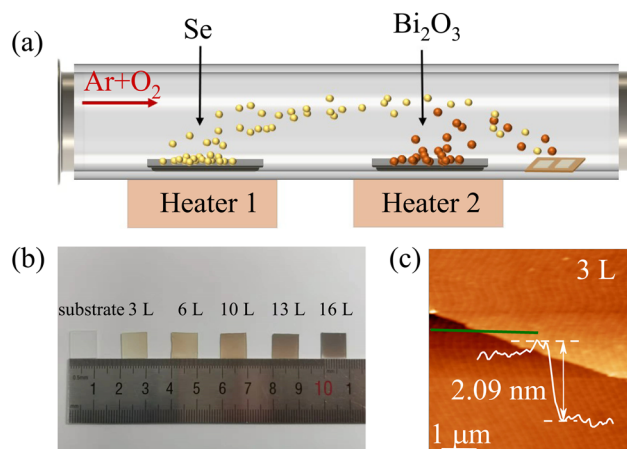


**Fig. 1** (a) The schematic diagram of the 2D $Bi_2O_2Se$ fabrication. (b) The optical picture of $Bi_2O_2Se$ films on the $1 \times 1$ cm² sapphire substrates. (c) The AFM image of the 3 L $Bi_2O_2Se$ film. The height profile along the green line is shown in the inset of the topographic map.

and 0.1 g of $Bi_2O_3$ powder (99.995%) were adopted as co-evaporation precursors to synthesize the $Bi_2O_2Se$ films. Argon mixed with oxygen was used as the growth carrier to transport the vapor precursor to the growth region through the whole growth process, while their flow rates were set as 200 and 5 s.c. c.m respectively. The Se metal and $Bi_2O_3$ powder were placed in low (about 573 K) and high temperature (973 K) centres, respectively. The sapphire substrate was placed downstream 5 cm away from the powder (about 773 K). The heating rate was set as 20 K min⁻¹. At such temperatures, the Se source melts and the $Bi_2O_3$ source sublimes. The high temperature of the substrate can facilitate the formation of nucleated $Bi_2O_2Se$ domains to find the most stable growth orientation and then promote the formation of a continuous $Bi_2O_2Se$ film at the centimetre scale. A small amount of oxygen gas is used to promote Se oxidation and balance the growth rate. To controllably synthesize the $Bi_2O_2$ Se thin film, the growth time was monitored from 3 to 20 min to fabricate 3 to 16 layers. Finally, the sample was allowed to naturally cool down to room temperature. The obtained films were labeled as 3 L, 6 L, 10 L, 13 L, and 16 L, respectively.

### Characterization techniques

The structure of $Bi_2O_2Se$ was determined by X-ray diffraction (XRD, Japan SmartLab) with a Cu Kα radiation source. The cross-sectional $Bi_2O_2Se$ lamella for high-resolution transmission electron microscopy (HRTEM) image was prepared by the focused ion beam method (FIB, Thermo Scientific Helio 5 CX). Then, the cross-sectional HRTEM images were obtained using the Thermo Scientific Talos F200X device. X-ray photoelectron spectroscopy (XPS, Escalab250Xi) was used to elucidate the valence states of Bi, Se, and O elements. The surface morphology and thickness of $Bi_2O_2Se$ films were measured by atomic force microscopy (AFM, Dimension Icon, Brucker). The transmittance spectra of all samples were recorded on an

Ultraviolet–visible near-infrared spectrophotometer (UV-vis-NIR, PerkinElmer Lambda 950) to confirm the electronic transition. Raman spectra were recorded on a micro-Raman spectrometer (Jobin–Yvon LabRAM HR 800 UV) in the frequency range of 130–200 cm$^{-1}$ with a 532 nm exciting laser. A Linkam THMSE 600 heating/cooling stage with a rate of 10 K min$^{-1}$ was used for temperature-dependent Raman measurements at 220–440 K. The polarized Raman spectra were recorded in backscattering geometry in parallel-polarized ($\theta V$) and cross-polarized ($\theta H$) scattering configurations to disclose the phonon anisotropy of 2D $Bi_2O_2Se$, where $\theta$ denotes the angle between the $y$ axis and the polarization direction. Spectroscopic ellipsometry (SE) experiments were performed by vertical variable-angle near infrared-ultraviolet optical ellipsometry (J. A. Woolam Co., Inc.) in the photon range from 0.49 to 5.00 eV. The incident angles were recorded at 60°, 65°, and 70° azimuthal orientation at room temperature while fixing at 70° in the temperature-dependent SE experiment. An Instec cell with a liquid nitrogen cooling accessory was employed in the temperature range of 230–470 K. All the fitting procedures were completed using the WVASE32 software package.[21]

### First-principles calculations

All calculations were performed using the Vienna *ab initio* simulation package (VASP). For the calculations of few-layer $Bi_2O_2Se$, the generalized gradient approximation of the Perdew–Burke–Ernzerhof functional was used for the exchange–correlation potential. The electronic interaction was employed with a kinetic energy cutoff of 400 eV. The $k$-point meshes (11 × 11 × 1) of Brillouin zones were sampled by the Monkhorst–Pack scheme. The total energy convergence criterion was set as 10$^{-5}$ eV.[22]

## Results and discussion

### Morphological and structural characterization

Centimeter-scale 2D $Bi_2O_2Se$ films were synthesized by a facile CVD method, as shown in Fig. 1a. In Fig. 1b, the $Bi_2O_2Se$ multilayers exhibit a deeper color with increasing thickness, representing stronger absorption in the visible spectral region. The flat surface that is observed using an optical microscope, as shown in Fig. S1,† confirms the good uniformity in large size films. In addition, the thicknesses of the $Bi_2O_2Se$ films have been determined by AFM, as displayed in Fig. 1c and Fig. S2.† The thickness for monolayer $Bi_2O_2Se$ has been reported as 6.08 Å[4] and the present layer numbers can be identified as 3–16 L.

$Bi_2O_2Se$ has a tetragonal phase with the $I4/mmm$ space group ($a = b = 3.88$ Å, $c = 12.16$ Å), as shown in the inset of Fig. 2a. In the layered 2D $Bi_2O_2Se$, two parts of 50% Se atoms in a $[Se]_n^{2n-}$ layer connect to the above and below $[Bi_2O_2]_n^{2n+}$ layers with the electrostatic force and then form a "zipper model".[23] Fig. 2a displays the XRD pattern of 16 L $Bi_2O_2Se$ at room temperature. The diffraction peaks at 14.75°, 29.68°, 44.74°, 60.86°, and 78.28° have been assigned to the (002),

(004), (006), (008), and (0010) planes (JPCDS#73-1316), respectively, which confirms that the tetragonal crystal phase of $Bi_2O_2Se$ was prepared.

To experimentally confirm the crystal structure and layer stacking of the 2D $Bi_2O_2Se$ film, extensive HRTEM measurements were performed. The cross-sectional TEM characterization of the $Bi_2O_2Se$/sapphire interface in Fig. 2b shows the definite epitaxy and lateral orientation relationship of $Bi_2O_2Se$ films on the sapphire substrate, which proves the high quality of the as-grown $Bi_2O_2Se$ film in this work. The thickness is determined to be about 9.89 nm by the magnified epitaxial alignment in Fig. 2c, which reveals the clear stratified structure with a 16 L film. The XPS spectrum of 16 L $Bi_2O_2Se$ displayed in Fig. S3† shows the existence of Bi, Se, and O atoms, and the exact peak positions of Bi 4p, Se 3d, and O 1s were accurately fitted. Fig. 2d shows that the 4f peak of the Bi element is split into well-defined 4f$_{7/2}$ and 4f$_{5/2}$ at binding energies of 158.5 eV and 163.8 eV, which correspond to the Bi$^{3+}$ state.[24] In addition, the separation between the peaks at 52.8 eV of Se 3d$_{5/2}$ and 53.7 eV of Se 3d$_{3/2}$ shown in Fig. 2e is 0.9 eV,[9] which can be verified from the Se$^{2-}$ state. The peaks of O 1s at 529.8 eV and 531.9 eV in Fig. 2f are also in good agreement with that from the O$^{2-}$ state.[16] Therefore, the concentration ratio of Bi : Se : O can be estimated to be ~2 : 1 : 2, suggesting that high-quality 2D $Bi_2O_2Se$ films were obtained.

According to the group-theoretical prediction, the $Bi_2O_2Se$ lattice follows the $D_{4h}$ point group symmetry with Raman-active optical modes of $A_{1g} + B_{1g} + 2E_g$. The two Raman-active modes of $B_{1g}$ and $A_{1g}$ are breathing modes, whereas the two $E_g$ modes belong to the interlayer shear modes.[23] The schematic diagram of the polarization configuration is shown in Fig. S4.† Only intrinsic $A_{1g}$ can be observed in Fig. 2g, which coincides with the high-quality $Bi_2O_2Se$ sample in the previous report.[16] The inset indicates that the $A_{1g}$ mode derives from the perpendicular movement of the Bi atom to the layers. Fig. 2h and Fig. S5a† indicate the relative intensity of the $A_{1g}$ phonon mode of $Bi_2O_2Se$ on the polar axis in the $\theta V$ and $\theta H$ configurations, respectively. According to the polarized Raman mappings (Fig. 2i and Fig. S5b in ESI†), the scattering intensity shows a period of 180° with a two-lobed shape under both polarization configurations. In particular, the minimum peak intensity occurs at about 90° and 270°, while the maximum value occurs at 0° and 180° with $\theta$–$V$ measurement. The opposite result is shown in the $\theta H$ measurement. Besides, the scattering intensity of the $A_{1g}$ mode is calculated to be proportional to $a^2 \cos^2 \theta$ and $a^2 \sin^2 \theta$ with $\theta V$ and $\theta H$ configurations, respectively, which can be seen in ESI Note 3.† As a result, the $A_{1g}$ mode shows the same polarization behavior from the theoretical and experimental aspects. Hence, the significant anisotropic phonon vibration indicates that 2D $Bi_2O_2Se$ is a good candidate for symmetry engineering, like polarization-sensitive optoelectronic applications.

### Layer-dependent lattice dynamics and dielectric functions

The layer-dependent phonon behavior of $Bi_2O_2Se$ is shown in Fig. 3a, and the fitted frequency and the full width at half
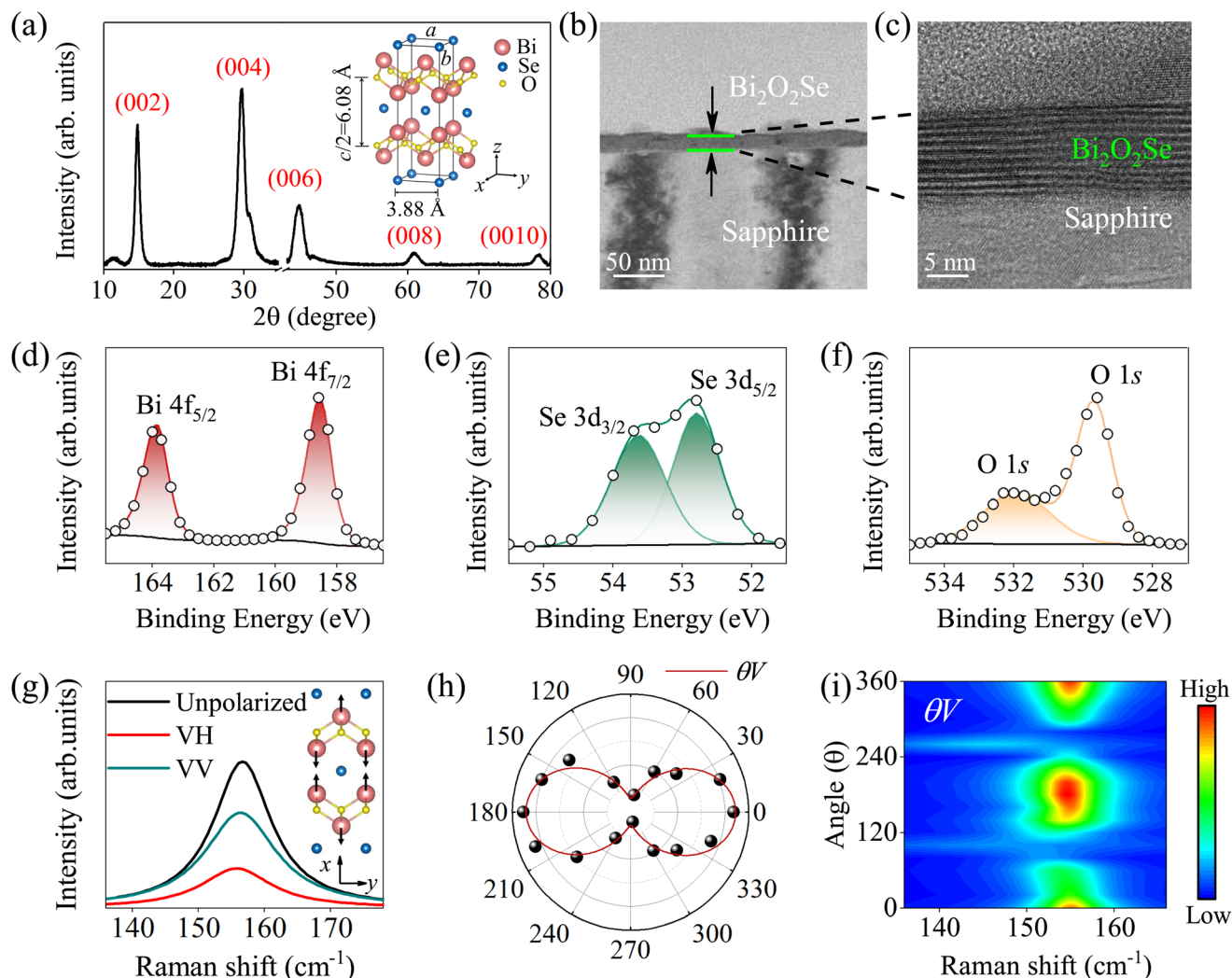
Fig. 2 (a) The XRD pattern of the 16 L $Bi_2O_2Se$ film. The inset is the crystal structure of $Bi_2O_2Se$. (b) The cross-sectional TEM characterization of the $Bi_2O_2Se$/Sapphire interface. (c) The magnified cross-sectional TEM image showing the high quality of the $Bi_2O_2Se$ film. The XPS spectra of (d) Bi 4f, (e) Se 3d, and (f) O 1s of the $Bi_2O_2Se$ film, respectively. (g) The unpolarized and polarized Raman spectra of the $Bi_2O_2Se$ film. The inset shows the atomic displacement diagram of the $A_{1g}$ Raman active mode. (h) The polar plots and fitted intensities of the $A_{1g}$ mode Raman as a function of angles with $\theta V$ configuration. (i) The polarized Raman mapping under $\theta V$ configuration.

maximum (FWHM) of the $A_{1g}$ mode are displayed in Fig. 3b. The frequency of 3 L $Bi_2O_2Se$ located at ~152 $cm^{-1}$ exhibits a sensitive blue shift to ~156 $cm^{-1}$ as the thickness increases to 16 L, which is consistent with the theoretical results.[15] The effective restoring forces acting on the Bi atom will weaken as the thickness decreases, since this mode can be contributed by out-of-plane vibrations of the Bi atom along the crystallo-graphic z-axis. In addition, the layer dependence of FWHM can also be observed in Fig. 3b. The reduced gradient of the Raman peak broadening implies a stronger phonon confine-ment effect and a decrease of the phonon lifetime of the $A_{1g}$ vibrational mode with increasing thickness. Moreover, the phonon broadening of the $A_{1g}$ peak in the finite size regime follows the phenomenological exponential format:[25,26] $\Pi_0(d) = \rho + \tau\exp(-d/\upsilon)$, where $\rho$, $\tau$, and $\upsilon$ are the fitting parameters and d represents the layer number of $Bi_2O_2Se$. This equation can

be well fitted with $\rho = 2.70$, $\tau = 24.47$, and $\upsilon = 12.25$, as shown in Fig. 3b. Note that the obtained format of the layer-depen-dent FWHM offers an additional reference for determining the thickness of the $Bi_2O_2Se$ material.

According to the transmittance spectra in Fig. 3c, the stron-ger absorption of the thicker layer is shown in the visible region, which is also consistent with the results in Fig. 1b. Moreover, the blue shift of the optical absorption edges from 16 L to 3 L demonstrates the enlarged band gap with decreas-ing thickness. As an indirect transition material, the Tauc formula can be expressed as $(\alpha\hbar\upsilon)^{1/2} \propto \hbar\upsilon - E_g$,[27] where $\alpha$, $\hbar\upsilon$, and $E_g$ are the absorption coefficient, photon energy and band gap, respectively. As a result, the optical band gap can be eval-uated to be ~1.23 eV for the 3 L film, as shown in the inset of Fig. 3c, while it shrinks gradually to ~1.01 eV for the 16 L film (Fig. S6†). In addition, three absorption peaks (labeled as A, B,
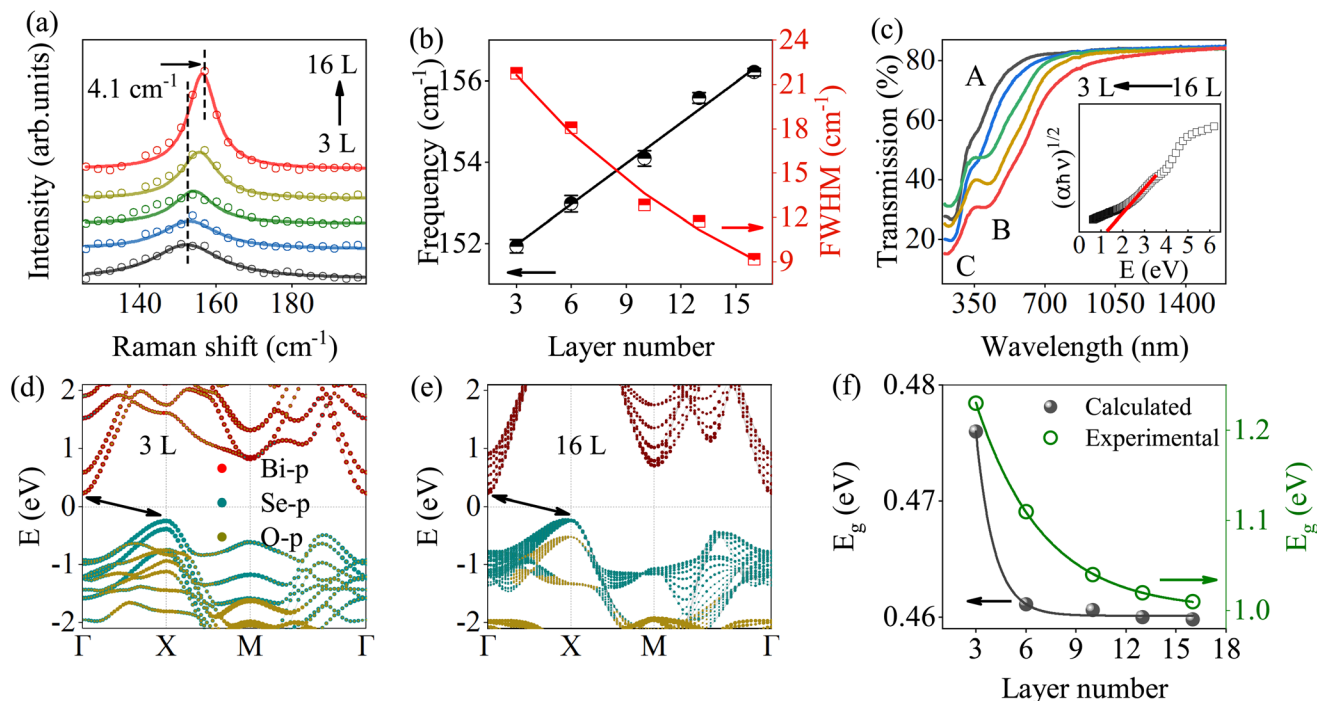
**Fig. 3** (a) The Raman spectra of 2D $Bi_2O_2Se$ films. (b) The layer-dependent frequency (circle) and FWHM value (square) of the $A_{1g}$ mode. (c) The transmittance spectra of $Bi_2O_2Se$ films. The inset shows the Tauc plot of the 3 L film. (d and e) The band structures of 3 L and 16 L $Bi_2O_2Se$ films. The dispersions of red, blue, and yellow circles represent the contributions by the Bi-p, Se-p, and O-p orbital respectively. (f) The evolution of the band gap with layer number by experiment (open) and calculation (solid).

and C) can be distinguished and their evolution with the layer number will be discussed in the following.

To discover the origin of layer-dependent electronic transition behavior, first-principles calculations of $Bi_2O_2Se$ films were performed. The conduction band minimum (CBM) at the Γ point is related to the Bi-p orbital. The valence band maximum (VBM) at the X point mainly contributes to the Se-p orbital and is independent of the thickness, as shown in Fig. 3d and e and Fig. S7.† When layers gradually stack to form a multilayer, the dispersion of the Bi-p orbital multiplies and the CBM moves towards the Fermi level energy, resulting in a band gap reduction from 0.50 eV of 2 L to 0.46 eV of 16 L $Bi_2O_2Se$. Due to the inherent defects of delocalization error and derivative discontinuity, the calculated band gap is underestimated compared with the experimental value.[28] However, it is still informative for the qualitative analysis of the band gap evolution with thickness. Therefore, the band dispersions in the present theoretical calculations are reasonable. Consequently, the consistent band gap trends of the calculation and experiment shown in Fig. 3f imply the enhanced electrostatic interactions in Bi–Se bonds with $Bi_2O_2Se$ layer stacking.

To satisfy the requirement of the quantitative design of the $Bi_2O_2Se$-based optical device, the dielectric functions were investigated by spectroscopic ellipsometry. A three-layer optical model (air/$Bi_2O_2Se$/sapphire) was constructed and the parameterized dispersive model consisting of Tauc–Lorentz and Lorentz oscillators was used for the fitting.[29–31] The fitted results are in good agreement with the obtained curves from $Bi_2O_2Se$, as shown in Fig. 4a, b and Fig. S9.† Besides, the similar thickness determined by SE and AFM in Table S1† also manifests the reliability of the present fitting results. The refractive index ($n$) and extinction coefficient ($k$) are displayed in Fig. S10g.† The real part ($\varepsilon_1$) and imaginary part ($\varepsilon_2$) in Fig. 4c and d of the dielectric function are transformed by optical constants. $\varepsilon_2$ presents the cross layer-dependent phenomenon, while the patterns can be roughly divided into two regions by the dashed line at 3.58 eV. Moreover, three obvious exciton peaks displayed in Fig. 4d labeled as $E_a$, $E_b$, and $E_c$ have been found, which are consistent with the experimental transmittance spectra.

The $\varepsilon_2$ magnitude at $E_a$ and $E_b$ increases with the layer number while showing an inverse trend at $E_c$. Such stronger optical absorption in the high-energy region of thinner $Bi_2O_2Se$ films is supposed to have potential use in ultraviolet detection. In contrast, the higher absorption in the low-energy region suggests that multilayers are more suitable for visible-near infrared detection. These interesting layer-dependencies can be understood with a quantum mechanism, which is related to the alternating domination of the excitonic effect and the joint density of states (JDOS) in 2D $Bi_2O_2$ Se layers. Actually, the imaginary part of the dielectric function can be expressed as $\varepsilon_2(E) = \gamma(\hbar e)^2 \mathrm{JDOS}|P_T|^2|U|^2 [(E_T - E)^2 + \gamma^2]^{-1} (m_0 E)^{-2}$, where $\hbar$ is the Planck constant, $|U|^2$ is according to
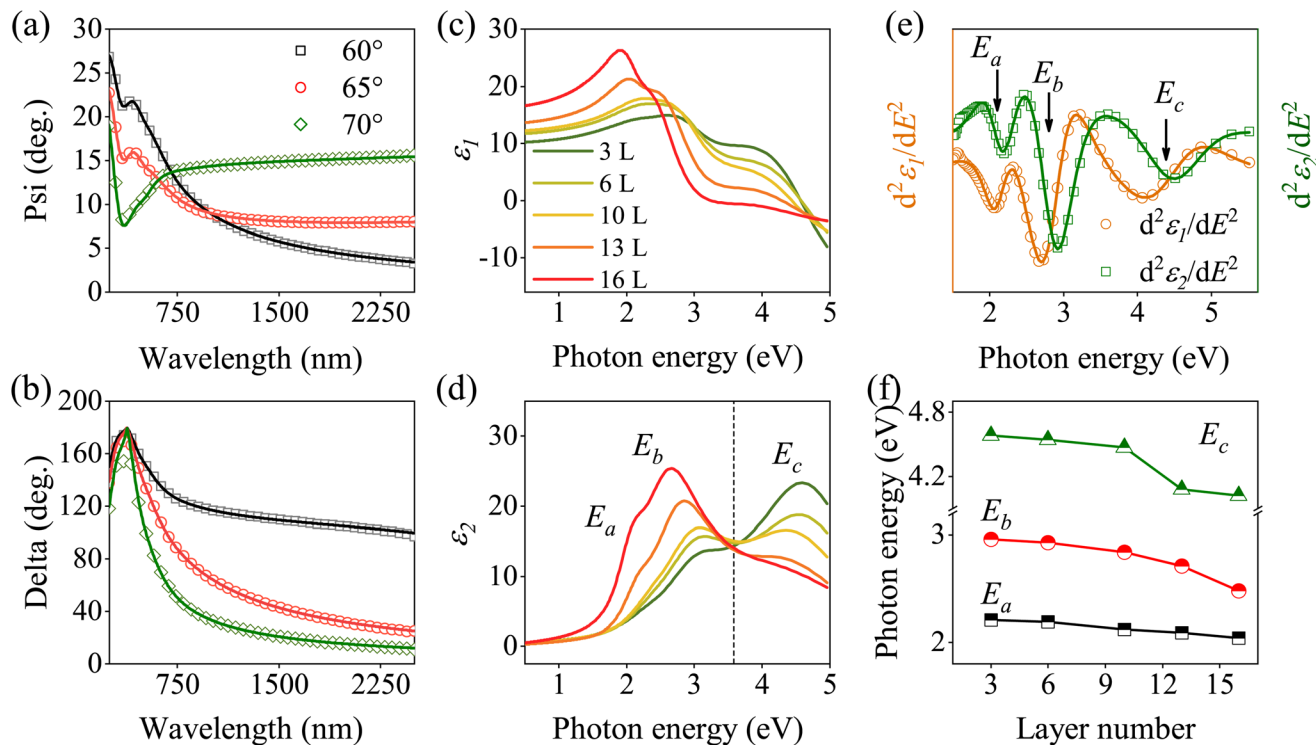
**Fig. 4** The measured (symbols) and best-fitted (lines) Psi (a) and Delta (b) curves of 10 L Bi$_2$O$_2$Se at 60°, 65°, and 70° azimuthal orientation, respectively. (c and d) The real parts and imaginary parts of dielectric function of Bi$_2$O$_2$Se films, respectively. (e) The second derivatives of the dielectric function spectra (symbols) and the best-fitted spectra (lines) of 10 L Bi$_2$O$_2$Se film. Three CPs including $E_a$, $E_b$, and $E_c$ are marked by arrows. (f) The layer-dependent center energies of three CPs.

the exciton effect of the interband transition, $\gamma$ is a damping coefficient and $m_0$ is the mass of a free electron. In addition, $E_T$ and $P_T$ are constant at specified excitation energy.[32] Hence, $\varepsilon_2$ is positively related to the JDOS and $|U|^2$, which means the variation of $\varepsilon_2$ can be explained by the competition of these two parameters.

In addition, the magnitude of the excitonic effect under a thermal equilibrium system can be evaluated from the exciton binding energy of the $n$th excitonic state,[33] $E^{(N)} = \frac{1}{2}\mu e^4[\hbar\varepsilon_N(N - \frac{1}{2})]^{-2}$, where $N$, $\mu$, and $\hbar$ represent the quantum number, the reduced mass of the exciton and the reduced Planck's constant, respectively. $\varepsilon_N$ is the $N$-dependent dielectric constant, which is positively correlated with the thickness of 2D materials. Therefore, the excitonic effect will decrease with increasing layer number. Moreover, as previously reported, the excitonic effect is more prominent in the ultraviolet region.[34] On the other hand, the JDOS represents the ability of the optical transition and exhibits a layer-dependent increase.[35] Therefore, the decussate pattern can be explained by the fact that the prevailing exciton effect in the few-layer Bi$_2$O$_2$Se leads to a higher $\varepsilon_2$ value in the high-energy region, while the increase of the JDOS with multilayer Bi$_2$O$_2$Se rapidly offsets the decaying exciton effect and dominates the increasing $\varepsilon_2$ value in the low-energy region. Besides, the acceleration of JDOS is reported to gradually decrease with increasing thickness, whereas a continuous upward trend is observed in

Bi$_2$O$_2$Se. It is caused by an additional positive effect, which may come from an increased mass density in thicker layers. The positive effect offsets the weakened acceleration of JDOS in the low-energy region and then contributes to the continuous up-trend $\varepsilon_2$ value at least up to the 16 L Bi$_2$O$_2$Se film. To sum up, the optical behavior of Bi$_2$O$_2$Se in the visible-near infrared region was derived from the combined effect of the JDOS and mass density. In contrast, the variation in the ultraviolet region was influenced by the exciton effect.

The standard critical point (SCP) model was used to reveal the corresponding center energies of three exciton peaks accurately.[36] In the vicinity of a critical point (CP), the dielectric functions can be represented via the SCP model as a phenomenological model which can be expressed as[37] $\varepsilon(E) = C_0 - A_m e^{i\varphi_m} (E - E_{cpm} + i\Gamma_m)^n$, where $m$ represents the oscillator number, $A_m$ is the amplitude, $\varphi_m$ is the excitonic phase angle, $E_{cpm}$ is the threshold energy and $\Gamma_m$ denotes the phenomenological broadening, respectively. The exponent $n$ characterizes the analytical shape of $\varepsilon(E)$ near its minima or maxima, which relates to the reduced masses of the electron and hole. The value of $n$ is $-1$, $-0.5$, $0$, and $0.5$ corresponding to the excitonic, one-dimensional, 2D, and three-dimensional critical points. In a 2D material system, the excitonic line-shape analysis ($n = -1$) always describes the optical transition well.[38] Furthermore, in order to eliminate the contribution of background emission, the second derivative of $\varepsilon(E)$ was used to

accurately determine the CP energies. The equation can be expressed as follows: $d^2\varepsilon/dE^2 = 2A_m e^{i\varphi_m}(E - E_{cpm} + i\Gamma_m)^{-3}$. The fitting parameters of the SCP model for $Bi_2O_2Se$ films are summarized in Table S2.† The center energies of three CPs of 10 L $Bi_2O_2Se$ are marked in Fig. 4e and the other fitting results can be seen in Fig. S11.† According to the SCP fitting results, two phenomena can be obtained. Firstly, the broadening $\Gamma_0$ of $E_a$ CP in Table S2† becomes narrow with layer-stacking, while the $\Gamma_2$ of $E_c$ CP becomes wider and the $\Gamma_3$ of $E_b$ remains almost invariable. Secondly, three CPs exhibit general red shifts with increasing layer number as shown in Fig. 4f. The default local electronic band structure of $Bi_2O_2Se$ includes the exciton binding energy and exciton transition energy, as shown in Fig. S12.† As mentioned above, the exciton binding energy of $Bi_2O_2Se$ will decrease with increasing layer number. Furthermore, the shrunk band gap derived from the orbital hybridization enhancement has already been proven from the transmittance spectra and the first-principles calculations. Therefore, the competition effect between the exciton binding energy and the band structure is observed. However, the domination of the former always has a remarkable effect on high-energy transitions and contributes to an obvious blue shift of CPs as the thickness increases,[39] which does not appear in the present results. Based on the above analysis, the red shifts of all CPs in $Bi_2O_2Se$ are dominated by the gradually shrinking original states of excitonic transitions with the enhanced interlayer interaction.

## Temperature-dependent lattice dynamics and dielectric functions

Temperature-dependent (220–440 K) Raman spectra of 3–16 L $Bi_2O_2Se$ films were obtained to clarify the thermal evolution of the $A_{1g}$ phonon behaviour. As shown in Fig. 5a and Fig. S8,† the frequency of the $A_{1g}$ mode in all films displays a continuous redshift with increasing temperature. In fact, the chemical bond relaxation relates to the bond length $d_Z = d_B\left(1 + \int_{T_0}^{T} \beta(t)dt + \int_{P_0}^{P} \zeta(P)dP\right)$ and the bond energy $E_Z = E_B - \int_{T_0}^{T} \eta(t)dt - \int_{V_0}^{V} P(V)dV$ in crystals,[40] where $\beta(t)$, $\zeta(P)$, and $\eta(t)$ are the thermal expansion coefficient, compression coefficient, and specific heat, respectively. In the pressure equilibrium system, the pressure-related parameters could be eliminated. Hence, the relationships indicate that increasing temperature will enhance the Bi–O bond length and weaken the bond energy in $Bi_2O_2Se$ crystals, thus leading to the softening phonon frequency with increasing temperature. Furthermore, to evaluate the temperature-sensibility of the Raman frequency, the temperature coefficient $\chi$ is determined,[41] which can be expressed as $\omega(T) = \omega_0 + \chi T$, where $\omega_0$ is the frequency of the $A_{1g}$ mode at 0 K, and $\chi$ represents the first-order temperature coefficient. As a result, the linearity of the Raman frequency as a function of temperature is shown in Fig. 5b. The absolute $\chi$ values of 2D $Bi_2O_2Se$ layers are obtained as 0.01722 cm$^{-1}$ K$^{-1}$, 0.01546 cm$^{-1}$ K$^{-1}$, 0.01407 cm$^{-1}$ K$^{-1}$, 0.01385 cm$^{-1}$ K$^{-1}$ and 0.01365 cm$^{-1}$ K$^{-1}$ for 3–16 L, respectively.
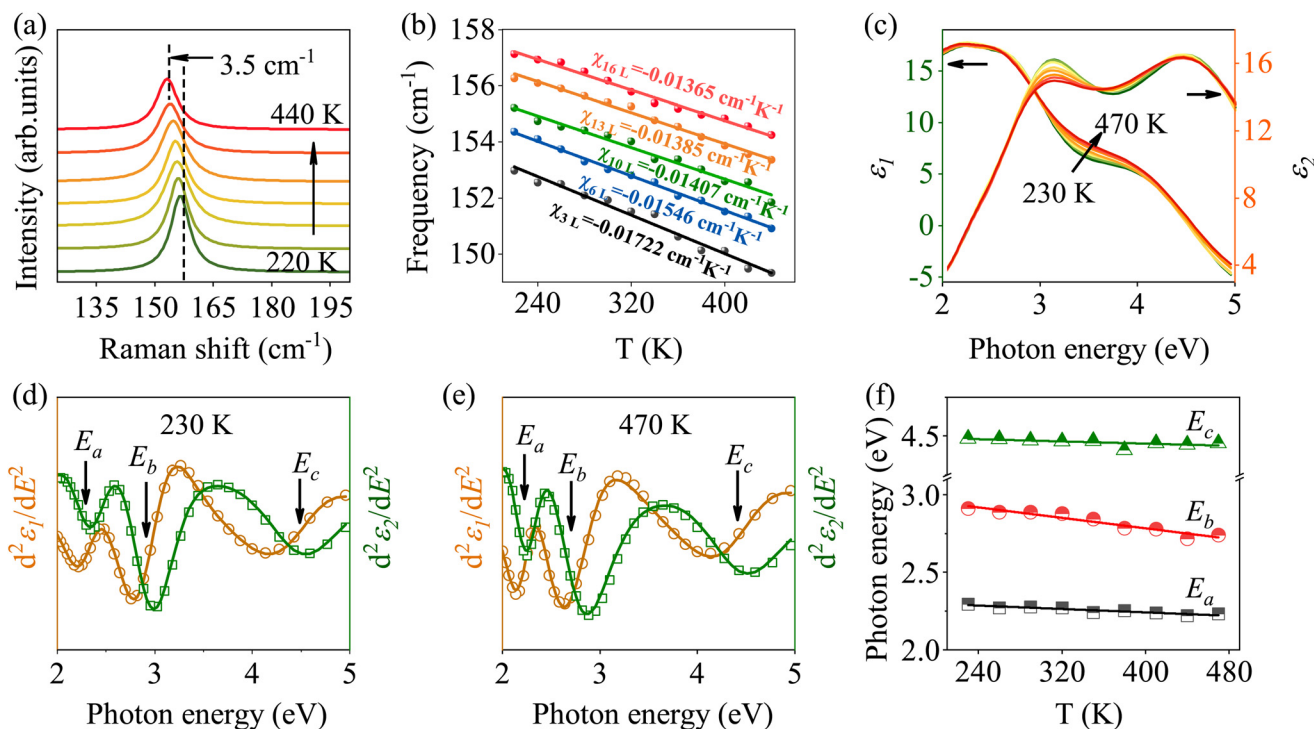


**Fig. 5** (a) The Raman spectra of 10 L $Bi_2O_2Se$ from 220 K–440 K. (b) Raman frequency *versus* temperature of the $A_{1g}$ mode from 3 L to 16 L $Bi_2O_2Se$ film. (c) The real parts and imaginary parts of the dielectric function of 10 L $Bi_2O_2Se$ in the range of 230 K–470 K. (d and e) The second derivatives of the dielectric function spectra (symbols) and the best-fitted spectra (lines) at 230 K and 470 K, respectively. The transition $E_a$, $E_b$, and $E_c$ CPs are marked by arrows. (f) The center energies of three CPs *versus* temperature.

The increased absolute $\chi$ value is accompanied by layer stacking. Moreover, the more sensitive $\chi$ value in the 2D system is larger than that of the $Bi_2O_2Se$ bulk ($0.01250$ cm$^{-1}$ K$^{-1}$),[42] which mainly derives from the weak interlayer interactions in thinner layers that lead to less vibrational restriction.

The temperature-dependent dielectric functions of 2D $Bi_2O_2Se$ were further investigated. The imaginary part of the dielectric function of 10 L at ~3 eV (the center energy of $E_b$ is 2.88 eV at 300 K) shows a significant reduction as the temperature increases in Fig. 5c, while it is negligible in other regions. Similar optical responses of the other 2D $Bi_2O_2Se$ films were also observed, as shown in Fig. S13–16.† From Fig. 5d and e, the typical CPs can be obtained using the SCP model and the parameters are listed in Table S3.† The center energies of three CPs were fitted with a linear equation in temperature dependence: $E(T) = E_L - \lambda T$, where $E_L$ is the adjustable parameter and $\lambda$ is the temperature coefficient $-dE/dT$. The obtained $\lambda$ values of 3–16 L $Bi_2O_2Se$ are listed in Table S4.† Three phenomena can be found. Firstly, the center energies of three CPs perform the negative correlation with increasing temperature, as seen in Fig. 5f. Similar to the $A_{1g}$ phonon thermal evolution, the Bi–Se bond length gradually increases with lattice expansion. The variation of lattice constants modifies the electronic band structure of $Bi_2O_2Se$, which contracts the original states of excitonic transitions and shrinks the exciton transition energy finally. However, the temperature-dependence of $E_c$ for 16 L $Bi_2O_2Se$ shows an inconsistent trend. Maybe the relatively wide broadening $\Gamma_2$ of the higher excitonic transition $E_c$ in the whole temperature range makes it difficult to be identified and accurately fitted (Fig. S16 and Table S4†). Therefore, the inconsistent trend of $E_c$ for 16 L $Bi_2O_2Se$ is reasonable. Secondly, the center energies of excitons exhibit layer-dependent temperature sensitivities. Specifically, the $\lambda$ values of $E_a$ and $E_b$ decrease sharply from 3–10 L and slow down as the layer number increases. The tendency is coincident with the layer-dependent interlayer interaction. Furthermore, the $\lambda$ value of the $E_b$ exciton is generally larger than those of $E_a$ and $E_c$, which indicates the stronger temperature-sensibility of the excitonic transition of $E_b$ and the significant changes of optical response in the corresponding wavelength range. These studies reveal the unique temperature-dependent optical absorption and exciton transition of the 2D $Bi_2O_2Se$ material in the broadband range, which is informative for temperature-related optical applications.

## Conclusions

In summary, centimeter-scale high-quality and layer-controlled 2D $Bi_2O_2Se$ films were prepared. The emergence of the stiffening phonon mode in thicker $Bi_2O_2Se$ layers can be interpreted by the enlarged Bi-p orbital dispersion as the thickness increases. Three excitons ($E_a$, $E_b$, and $E_c$) are precisely observed and exhibit red shifts with layer stacking. Due to the combined effect of the JDOS and mass density, the imaginary part of the dielectric functions in $E_a$ and $E_b$ (visible-near infrared region)

increases as the thickness increases. In contrast, the dominated exciton effect induces a layer-dependent decrease in $E_c$ (ultraviolet region). Besides, the temperature-sensibilities of the phonon frequency and exciton transition energies exhibit remarkable layer-dependencies, which are informative for temperature-related technologies. In particular, the optical response of the $E_b$ exciton exhibits a significant dependence on temperature, which suggests a promising optical modulation of 2D $Bi_2O_2Se$ at the corresponding wavelength by temperature. Overall, the present work is expected to promote the physical understanding of the phonon dynamics, dielectric properties, and electronic structure of 2D $Bi_2O_2Se$, which are helpful for $Bi_2O_2Se$-related high-performance optoelectronic device designing.

## Author contributions

Y. F. Li and K. Dai contributed equally to this work. Y. F. Li, K. Dai, and Z. G. Hu initiated and designed the experiments and wrote the manuscript. Y. F. Li, K. Dai, J. Z. Zhang, and K. Jiang provided sufficient discussion about XRD, Raman, and SE data. L.C. Gao performed the calculations. A. Y. Cui, Y. W. Li, L. Y. Shang, and L. Q. Zhu conducted the experiments of sample fabrication. Y. F. Li, K. Dai, and J. Z. Zhong gave the detailed analyses of the underlying mechanism. All authors discussed the results and commented on the manuscript.

## Conflicts of interest

The authors declare no competing financial interest.

## Acknowledgements

## References

1 J. W. Lee, Z. Dai, T. H. Han, C. Choi, S. Y. Chang, S. J. Lee, N. De Marco, H. Zhao, P. Sun, Y. Huang and Y. Yang, *Nat. Commun.*, 2018, **9**, 3021.

2 R. Han, S. Feng, D. M. Sun and H. M. Cheng, *Sci. China Inf. Sci.*, 2021, **64**, 140402.

3 L. Wang, D. Xu, L. Jiang, J. Gao, Z. Tang, Y. Xu, X. Chen and H. Zhang, *Adv. Funct. Mater.*, 2021, **31**, 2004408.

4 J. X. Wu, H. T. Yuan, M. M. Meng, C. Chen, Y. Sun, Z. Y. Chen, W. H. Dang, C. W. Wu, Y. J. Liu, J. B. Yin, Y. B. Zhou, S. Y. Huang, H. Q. Xu, Y. Cui, H. Y. Hwang, Z. F. Liu, Y. L. Chen, B. H. Yan and H. L. Peng, *Nat. Nanotechnol.*, 2017, **12**, 530–534.

5 J. B. Yin, Z. J. Tan, H. Hong, J. X. Wu, H. T. Yuan, Y. J. Liu, C. Chen, C. W. Tan, F. R. Yao, T. R. Li, Y. L. Chen, Z. F. Liu, K. H. Liu and H. L. Peng, *Nat. Commun.*, 2018, **9**, 3311.

6 C. Chen, M. X. Wang, J. X. Wu, H. X. Fu, H. F. Yang, Z. Tian, T. Tu, H. Peng, Y. Sun, X. Xu, J. Jiang, N. B. M. Schröter, Y. W. Li, D. Peng, S. Liu, S. A. Ekahana, H. T. Yuan, J. M. Xue, G. Li, J. F. Jia, Z. K. Liu, B. H. Yan, H. L. Peng and Y. L. Chen, *Sci. Adv.*, 2018, **4**, eaat8355.

7 P. Luo, F. K. Wang, J. Y. Qu, K. L. Liu, X. Z. Hu, K. W. Liu and T. Y. Zhai, *Adv. Funct. Mater.*, 2021, **31**, 2008351.

8 C. Fan, B. B. Dai, H. K. Liang, X. Xu, Z. D. Qi, H. T. Jiang, H. G. Duan and Q. L. Zhang, *Adv. Funct. Mater.*, 2021, **31**, 2010263.

9 M. T. Hossain, M. Das, J. Ghosh, S. Ghosh and P. K. Giri, *Nanoscale*, 2021, **13**, 14945–14959.

10 D. Vrushabendrakumar, H. Rajashekhar, S. Riddell, A. P. Kalra, K. M. Alam and K. Shankar, *Nanotechnology*, 2021, **32**, 485602.

11 M. Kang, H. J. Chai, H. B. Jeong, C. Park, I. Jung, E. Park, M. M. Cicek, I. J. Lee, B. S. Bae, E. Durgun, J. Y. Kwak, S. Song, S. Y. Choi, H. Y. Jeong and K. Kang, *ACS Nano*, 2012, **15**, 8715–8723.

12 Y. F. Chen, W. L. Ma, C. W. Tan, M. Luo, W. Zhou, N. J. Yao, H. Wang, L. L. Zhang, T. F. Xu, T. Tong, Y. Zhou, Y. B. Xu, C. H. Yu, C. H. Yu, C. X. Shan, H. L. Peng, F. Y. Yue, P. Wang, Z. M. Huang and W. D. Hu, *Adv. Funct. Mater.*, 2021, **31**, 2009554.

13 P. Luo, F. W. Zhuge, F. K. Wang, L. Y. Lian, K. L. Liu, J. B. Zhang and T. Y. Zhai, *ACS Nano*, 2019, **13**, 9028–9037.

14 Q. D. Fu, C. Zhu, X. X. Zhao, X. L. Wang, A. Chaturvedi, C. Zhu, X. W. Wang, Q. S. Zeng, J. D. Zhou, F. C. Liu, B. K. Tay, H. Zhang, S. J. Pennycook and Z. Liu, *Adv. Mater.*, 2019, **31**, 1804945.

15 T. Cheng, C. W. Tan, S. Q. Zhang, T. Tu, H. L. Peng and Z. R. Liu, *J. Phys. Chem. C*, 2018, **122**, 19970–19980.

16 J. X. Wu, C. W. Tan, Z. J. Tan, Y. J. Liu, J. B. Yin, W. H. Dang, M. Z. Wang and H. L. Peng, *Nano Lett.*, 2017, **17**, 3021–3026.

17 J. Liang, T. Tu, G. C. Chen, Y. W. Sun, R. X. Qiao, H. Ma, W. T. Yu, X. Zhou, C. J. Ma, P. Gao, H. L. Peng, K. H. Liu and D. P. Yu, *Adv. Mater.*, 2020, **32**, 2002831.

18 L. Pan, L. Zhao, X. X. Zhang, C. C. Chen, P. P. Yao, C. L. Jiang, X. D. Shen, Y. N. Lyu, C. H. Lu, L. D. Zhao and Y. F. Wang, *ACS Appl. Mater. Interfaces*, 2019, **11**, 21603–21609.

19 L. Pan, W. D. Liu, J. Y. Zhang, X. L. Shi, H. Gao, Q. F. Liu, X. D. Shen, C. H. Lu, Y. F. Wang and Z. G. Chen, *Nano Energy*, 2020, **69**, 104394.

20 J. Li, Z. X. Wang, Y. Wen, J. W. Chu, L. Yin, R. Q. Cheng, L. Lei, P. He, C. Jiang, L. P. Feng and H. Jun, *Adv. Funct. Mater.*, 2018, **28**, 1706437.

21 J. A. Woollam, *Gudie to using WVASE32*, Lincoln, 2008.

22 B. Zhou, A. Y. Cui, L. C. Gao, K. Jiang, L. Y. Shang, J. Z. Zhang, Y. W. Li, S. J. Gong, Z. G. Hu and J. H. Chu, *Phys. Rev. Mater.*, 2021, **5**, 125404.

23 Q. L. Wei, R. P. Li, C. Q. Lin, A. L. Han, A. M. Nie, Y. R. Li, L. J. Li, Y. C. Cheng and W. Huang, *ACS Nano*, 2019, **13**, 13439–13444.

24 M. A. Hughes, Y. Fedorenko, B. Gholipour, J. Yao, T. H. Lee, M. G. Russell, K. P. Homewood, S. Hinder, D. W. Hewak, S. R. Elliott and R. J. Curry, *Nat. Commun.*, 2014, **5**, 5346.

25 S. L. Zhang, S. N. Wu, Y. Yan, T. Hu, J. Zhao, Y. Song, Q. Qu and W. Ding, *J. Raman Spectrosc.*, 2008, **39**, 1578–1583.

26 F. Wang, B. Zhou, H. M. Sun, A. Y. Cui, T. Jiang, L. P. Xu, K. Jiang, L. Y. Shang, Z. G. Hu and J. H. Chu, *Phys. Rev. B*, 2018, **98**, 245403.

27 J. Tauc, *Mater. Res. Bull.*, 1968, **3**, 37–46.

28 S. V. Eremeev, Y. M. Koroteew and E. V. Chulkov, *Phys. Rev. B*, 2019, **100**, 115417.

29 A. B. Djurišić, Y. Chan and E. H. Li, *Mater. Sci. Eng., R*, 2002, **38**, 237–293.

30 A. S. Ferlauto, G. M. Ferreira, J. M. Pearce, C. R. Wronski, R. W. Collins, X. Deng and G. Ganguly, *J. Appl. Phys.*, 2002, **92**, 2424.

31 M. Z. Xie, M. Li, L. M. Li, J. Z. Zhang, K. Jiang, L. Y. Shang, Y. W. Li, Z. G. Hu and J. H. Chu, *Appl. Phys. Lett.*, 2020, **117**, 102101.

32 P. Y. Yu and M. Cardona, *Fundamentals of Semiconductors Physics and Materials Properties*, Springer, Berlin, 2010.

33 A. Chernikov, T. C. Berkelbach, H. M. Hill, A. Rigosi, Y. L. Li, O. B. Aslan, D. R. Reichman, M. S. Hybertsen and T. F. Heinz, *Phys. Rev. Lett.*, 2014, **113**, 076802.

34 M. Y. Wei, J. Lian, Y. Zhang, C. L. Wang, Y. M. Wang and Z. Xu, *npj 2D Mater. Appl.*, 2022, **6**, 1.

35 Y. L. Yu, Y. F. Yu, Y. Q. Cai, W. Li, A. Gurarslan, H. Peelaers, D. E. Aspnes, C. G. V. d. Walle, N. V. Nguyen, Y. W. Zhang and L. Y. Cao, *Sci. Rep.*, 2015, **5**, 16996.

36 P. Lautenschlager, M. Garriga, L. Vina and M. Cardona, *Phys. Rev. B: Condens. Matter Mater. Phys.*, 1987, **36**, 4821.

37 W. Li, A. G. Birdwell, M. Amani, R. A. Burke, X. Ling, Y. H. Lee, X. L. Liang, L. M. Peng, C. A. Richter, J. Kong, D. J. Gundlach and N. V. Nguyen, *Phys. Rev. B: Condens. Matter Mater. Phys.*, 2014, **90**, 195434.

38 X. D. Zhu, J. B. He, R. J. Zhang, C. X. Cong, Y. X. Zheng, H. Zhang, S. W. Zhang and L. Y. Chen, *Nanoscale*, 2020, **12**, 23732.

39 M. S. Fang, Z. Y. Wang, H. G. Gu, M. Y. Tong, B. K. Song, X. N. Xie, T. Zhou, X. G. Chen, H. Jiang, T. Jiang and S. Y. Liu, *Appl. Surf. Sci.*, 2020, **509**, 144822.

40 X. Ling, L. B. Liang, S. X. Huang, A. A. Puretzky, D. B. Geohegan, B. G. Sumpter, J. Kong, V. Meunier and M. S. Dresselhaus, *Nano Lett.*, 2015, **15**, 4080–4088.

41 E. S. Zouboulis and M. Grimsditch, *Phys. Rev. B: Condens. Matter Mater. Phys.*, 1991, **43**, 12490.

42 F. Yang, R. D. Wang, W. W. Zhao, J. Jiang, X. Wei, T. Zheng, Y. T. Yang, X. W. Wang, J. P. Lu and Z. H. Ni, *Appl. Phys. Lett.*, 2019, **115**, 193103.